Sub-surface imaging of soiled cotton fabric using full-field optical coherence tomography

ZIJIAN ZHANG,[1] UYAI IKPATT,[2] SAMUEL LAWMAN,[1,3] BRYAN WILLIAMS,[3] YALIN ZHENG,[3] HUNGYEN LIN,[4] AND YAOCHUN SHEN,[1,*]

[1]*Department of Electrical Engineering and Electronics, University of Liverpool, Liverpool L69 3GJ, United Kingdom*
[2]*Unilever R & D Port Sunlight, Bebington CH63 3JW, United Kingdom*
[3]*Department of Eye and Vision Science, University of Liverpool, Liverpool L7 8TX, United Kingdom*
[4]*Department of Engineering, Lancaster University, Lancaster LA1 4YW, United Kingdom*
*Y.C.Shen@liverpool.ac.uk

Abstract: In the laundry industry, colorimetry is a common way to evaluate the stain removal efficiency of detergents and cleaning products. For ease of visualization, the soiling agent is treated with a dye before measurement. However, it effectively measures the dye removal rather than stain removal and it cannot provide depth-resolved information of the sample. In this study, we show that full-field (FF) optical coherence tomography (OCT) technique is capable of measuring the cleaning effect on cotton fabric by imaging the sub-surface features of fabric samples. We used a broadband light-emitting diode (LED) source to power the FF-OCT system that achieves the resolution of 1 μm axially and 1.6 μm laterally. This allows the micron-sized cotton fibres/fibrils at different depth positions to be resolved. The clean, the soiled and the washed samples can be differentiated from their cross-sectional images using OCT, where the cleaning effect can be correlated with the sub-surface fibre volume. The experimental results of the proposed method were found to be in good agreement with those of the standard colorimetry method. The proposed technique therefore offers an alternative way for measuring the stain removal from fabric substrate to assess the effectiveness of laundry detergent products.

1. Introduction

The ability to measure and monitor the removal of semi-solid fats or oils from substrates is important for the assessment of the effectiveness of the current surfactant systems for stain removal. Colorimetry, the science of color measurement, has been widely employed for wash studies to quantify color and to derive color differences from the soiled samples before and after washing [1–3]. The technique is based on the tristimulus theory of color vision, which states that the human eye possesses receptors for three primary colors and all colors can be regarded as mixtures of these primaries [4]. The colors of tested fabric can be measured by using a spectrophotometer and recorded numerically in terms of color formulae such as the CIE $L^*a^*b^*$ (known as CIELAB) color space. This colorimetric method is easy to use, but it requires the stains or soils to be colored for the level of removal to be measured. As a result, the ΔE^* (delta E) values (defined as the difference between two colors) corresponding to washed and unwashed samples, as well as washed and unsoiled samples, represent the criteria for the stain removal efficiency. Although the chosen dyes are soluble in the stains or soil which are investigated, the colorimetry method is however still an indirect method of measuring stain removal as it effectively measures dye removal. The colorimetry method does not provide depth-resolved information of the sample either.

Optical coherence tomography (OCT) is a non-invasive and non-contact optical technology that is able to generate the depth profiles of measured samples [5]. It was primarily developed and used for ophthalmic applications but has been gaining interest in the field of non-invasive

testing. Examples of previously demonstrated applications span from the art diagnostics [6,7], polymers [8,9], sub-surface defect detection [10,11], pharmaceutical film coatings [12–14], automotive paints analysis [15,16], and the investigation of silicon integrated circuits [17]. Imaging with OCT is based on the principle of low-coherence interferometry and is typically achieved with Michelson interferometer. The imaging modality decouples the axial and lateral resolution, where the former is ultimately limited by the temporal coherence of the illumination source, while the latter is primarily determined by the numerical aperture (NA) of the objective [18]. Researchers have focused on the development of full-field optical coherence tomography (FF-OCT) in order to generate a three-dimensional (3D) datacube using a charge-coupled device (CCD) or complementary metal-oxide-semiconductor (CMOS) camera and a single axis scan in the sample depth direction [19,20]. In comparison to conventional flying-spot OCT systems where 3D imaging was obtained by raster scanning over the sample in both x- and y-lateral directions, time-domain FF-OCT is naturally suited for obtaining high lateral and axial resolution 3D datacube with a single z-direction scan, due to focus position being scanned simultaneously with probed depth and efficient use of low cost broadband spatially incoherence light source, respectively. It should be noted that spatial coherence can play a critical role in FF-OCT performance, especially for the FF-OCT systems that employs high-NA (such as NA > 0.5) microscope objectives for their interferometer arms [21,22]. In this case, the axial resolution is no longer dominated by the temporal coherence but the longitudinal spatial coherence, and it is possible to use of relatively narrowband source to drive a FF-OCT to achieve high resolutions axially and laterally [23].

Phase stepping and shifting methods are the most popular reconstruction strategy for FF-OCT, which are used to extract the interference signal [24–26]. Several authors reported their FF-OCT systems which used a piezoelectric stage actuator (PZT) to generate oscillation at reference arm. Three or four-phase-stepped images were acquired with the displacements of the reference mirror and used for the reconstruction of OCT images. The requirement of usually more than three interferograms at each phase shifting position limits the operation speed of the system. A number of studies have been reported to increase the imaging efficiency with sophisticated hardware based (optical or electrical) implementations. For example, Dubois et al [27], proposed an FF-OCT system based on lock-in detection technique, where a photo-elastic birefringence modulator was used to generate a sinusoidal phase shift between the sample and reference waves, four original interferograms can be recorded successively and then demodulated to an OCT image. Akiba et al [28], proposed a heterodyne detection technique, where two synchronised CCD cameras were used to simultaneously acquire two quadrature and direct-current (DC) images to obtain an OCT image. Sato et al [29], introduced Wollaston prism to realise optical Hilbert transform, in which the interferograms of four phase shifts were reduced to two acquisitions.

In previous studies [13,15] we have instead used continuous scanned acquisition and software-based image reconstruction methods for FF-OCT. Here we develop the method further exploit its resolution potential, giving "micro-OCT" [30] (approximate 1-μm lateral and axial resolution) or ultrahigh-resolution (UHR) [31] performance. The measurement can continuously operate without employing any component to generate phase information for retrieving tomography images. The whole system configuration is similar to the compact arrangement of "vertical scanning interferometer" [32] widely used for measuring surface profiles with demonstrated simplicity and flexibility in industrial environments.

In this study, we demonstrate for the first time that FF-OCT is able to resolve the removal of oily and fatty stains in fabrics, which have been subjected to cleaning processes. To do this, we used our FF-OCT system to acquire a series of OCT images of fabric samples, which have undergone a controlled staining and cleaning processes, at a 1-μm and 1.6-μm axial and lateral resolutions, respectively, in order to provide sub-surface information to evaluate cleaning effect. The technique results were verified by the current gold standard method of colorimetry, but also shown to be work without the dying of some stains required by colorimetry.

2. Materials and methods

2.1 Method

A 3D datacube can be acquired through single scanning imaging in the sample's axial direction for the FF-OCT modality, where a CCD/CMOS camera is used to record a series of two-dimensional (2D) interferograms (x-y plane) to form the 3D datacube. The imaging scheme can be mathematically expressed as Eq. (1) when considering a time-domain OCT (TD-OCT) imaging theory [33].

$$I_{FF-OCT}(x,y,\Delta z) = \int S(\omega)\left(R_{Ref}(x,y) + \sum_{i=1}^{N} R_{Sampl-i\mathrm{th}}(x,y) + \right.$$
$$\left. 2\sum_{i=1}^{N} \sqrt{R_{Ref}(x,y)R_{Sampl-i\mathrm{th}}(x,y)} \cos[\phi(x,y,\Delta z)] \right) d\omega \tag{1}$$

where $S(\omega)$ represents the intensity spectrum of a Gaussian shaped light source as a function of frequency ω, R_{Ref} is the reflectivity of a reference mirror and $R_{Sampl-i\mathrm{th}}$ is the reflectivity of the i-th reflector of a sample with N layers. In addition, $\phi(x,y,\Delta z)$ represents the phase changes when translating either the reference arm or the sample arm by a geometry distance Δz. The light echoes from different reflectors within the sample and the positions of the reference mirror give rise to time delay information. The recorded signal intensity consists of three components over the integrated source spectrum, which are DC offset, cross-correlation signal and auto-correlation signal. DC offset is due to the reflectivity from both the two interferometer arms. Cross-correlation signal is generated with the interference between the reference mirror and the sample reflectors at multiple depths. Auto-correlation signal results from the interference between the different sample reflectors, which has been ignored in Eq. (1) since it is independent of the moving distance Δz. Eq. (1) can be rewritten as the sum of the DC signal and the cross-correlation signal intensities as

$$I_{FF-OCT}(x,y,\Delta z) = I_{DC}(x,y) + I_{Cross}(x,y,\Delta z)\cos\phi(x,y,\Delta z) \tag{2}$$

Phase-shift method is a common method of FF-OCT image reconstruction, where phase shifting is implemented by oscillating the reference arm using a PZT. At each scanned depth position, four interferograms and their corresponding phase-shift steps $\ell = 0,1,2,3$ are acquired, which can be written as Eq. (3)

$$I_{FF-OCT}^{\ell}(x,y,\Delta z) = I_{DC}(x,y) + I_{Cross}(x,y,\Delta z)\cos\left(\phi(x,y,\Delta z) + \frac{\ell\pi}{2} \right) \tag{3}$$

A number of *en-face* images can be reconstructed to form a 3D OCT datacube with Eq. (4)

$$I_{Cross}(x,y,\Delta z) \propto \left[I_{FF-OCT}^{\ell=0} - I_{FF-OCT}^{\ell=2} \right]^2 + \left[I_{FF-OCT}^{\ell=1} - I_{FF-OCT}^{\ell=3} \right]^2 \tag{4}$$

In our proposed imaging scheme, a series of 2D interferograms along the axial direction are captured continuously to form the raw 3D datacube by employing a high-precision linear stage to translate the sample at a nanoscale sampling interval. Even though this would require extensive hardware storage, it nevertheless reduces hardware complexity since only a motorised stage is required for experiment. The image reconstruction task is converted from retrieving a series of *en-face* images to demodulating tomography signals (A-scans), which allows the use of postprocessing methods for image reconstruction.

We introduce a normalised mirror signal, denoted as $I_{Mirror}(\Delta z')$, which is generated by measuring the surface of a flat mirror with the same scanning step as the measurement performed on a sample. By convolving the mirror signal with the raw A-scan signals, it effectively functions as a weighted average filter to remove the DC offset while amplifying the cross-correlation signal. This step can be expressed as Eq. (5)

$$I'_{FF-OCT}(x,y,\Delta z) = I_{FF-OCT}(x,y,\Delta z) \otimes I_{Mirror}(\Delta z') \tag{5}$$

where '⊗' represents the convolution operator. Further, by taking Hilbert transform, denoted by $H\{\}$, all the A-scan signals can be demodulated to form the reconstructed OCT datacube, which is written as Eq. (6)

$$I'_{Cross}(x,y,\Delta z) = \sqrt{\left[I'_{FF-OCT}(x,y,\Delta z)\right]^2 + \left[H\{I'_{FF-OCT}(x,y,\Delta z)\}\right]^2} \qquad (6)$$

It should be noted that practical signal demodulation is performed using a multithreaded process, where the size of the demodulated signals is one-tenth of the original ones after resampling. Thus, the reconstruction time for a sample volume of $100 \times 100 \times 1000$ pixels takes approximately ten seconds while freeing up over 20 MB of data storage.

As a further illustration, we simulated a time-domain interferogram corresponding to a sample with three layers, and an additive white Gaussian noise was applied to the original signal, as shown in Fig. 1(a). The simulated source had a Gaussian-shape spectrum centred at 600 nm with an full-width-at-half-maximum (FWHM) of 200 nm (see Fig. 1(b)), consistent with sources typically used in UHR FF-OCT. Figure 1(c) shows a simulated mirror interferogram after intensity normalisation, where the measured FWHW was 0.8 μm that represents the axial resolution determined by the broadband source. In order to assess the proposed reconstruction method, the depth information of the sample (Fig. 1(a)) was reconstructed by using the classic phase-shift method at four shifted phase positions. As shown in Fig. 1(d), the solid blue line is the A-scan which uses the single image at each quarter position for reconstruction. The yellow, green, and red solid lines in Fig. 1(d) are the reconstructed A-scans that correspond to 20, 50 and 100 accumulated images per phase-shift, respectively, in which increased signal-to-noise ratio (SNR) can be observed. The solid black line in Fig. 1(d) shows that A-scan reconstructed using the proposed method closely resembles to the A-scan using the classic phase-shift method. The FWHM measured from the A-scan (solid black line) is approximate 1 μm in close agreement with the theoretically axial resolution (0.8 μm).
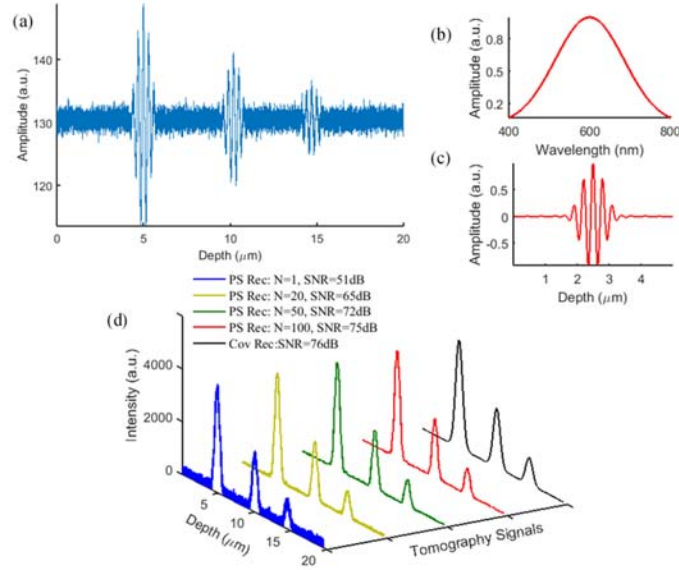

Fig. 1. Simulation of the proposed FF-OCT image reconstruction scheme. (a) Simulated sample signal with three layers. (b) Simulated light source spectrum centred at 600 nm and an FWHM of 200 nm. (c) Simulated mirror interference signal. (d) Reconstructed A-scan (blue) based on the four-step phase-shift (PS) method and the A-scans after averaging N signals to enhance SNR (yellow: N=20; green: N=50; red: N=100), compared with the A-scan reconstructed using the proposed method (black).

2.2 System setup

Based on the proposed method, a FF-OCT system can be designed with a fewer optical and electrical components. Figure 2 shows the schematic diagram of our FF-OCT system setup driven by a broadband LED source (Thorlabs, MBB1L3, wavelength range 470–850 nm), where the incident beam splits into the two arms by a non-polarizing 50/50 beamsplitter (BS). Like a Linnik-type FF-OCT, there are two nearly identical microscope objectives (Nikon, 10X, 0.3 numerical aperture) operating on both the reference and the sample arms. The reflected (mainly from reference arm) and backscattered light (mainly from the measured sample) and their interference are registered on an sCMOS camera (Andor Technology, Zyla 5.5) after being focused by a plano-convex lens (200-mm focal length). Due to the low temporal coherence of the light source, interference occurs only when the optical path difference (OPD) between the two arms is within the coherence length. By translating the sample along the z-axis with a high-precision motorised stage (PI MICOS, LPS-65), a stack of raw 2D interferograms at various scanning depths are acquired yielding a raw 3D datacube. During the measurement, each fabric sample is fixed onto a kinematic mount in the sample arm by using double-sided tape. A custom-built imaging control and data analysis software is used to perform the measurements and reconstruct the 3D OCT datacube in Matlab.
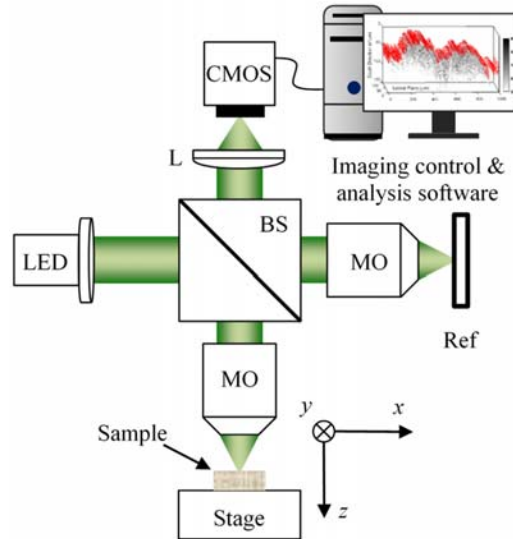

Fig. 2. Schematic diagram of the FF-OCT setup. LED - broadband LED light source; BS – beam splitter; MO - microscope objectives; Ref - reference mirror; L - plano-convex lens.

2.3 Resolution performance

For the LED source, the effective spectrum is verified by using a spectrometer (Ocean Optics, USB 2000+) centred at 590 nm with an FWHM of 200 nm. The theoretically axial resolution is calculated to be approximately 0.77 μm in air, using Gaussian approximation [34] and practically measuring a mirror reflection. The intensity profile after normalisation is shown in Fig. 3(a). By applying the proposed reconstruction method to demodulate its corresponding envelope signal, the achieved axial resolution is approximately 1 μm. The lateral resolution of a diffraction-limited system can be defined by the point spread function (PSF) and can be determined by measuring a standard test target USAF 1951, thus yielding the system's edge profile. The FWHM taken is 1.6 μm as compared to a theoretical value of 1.25 μm.
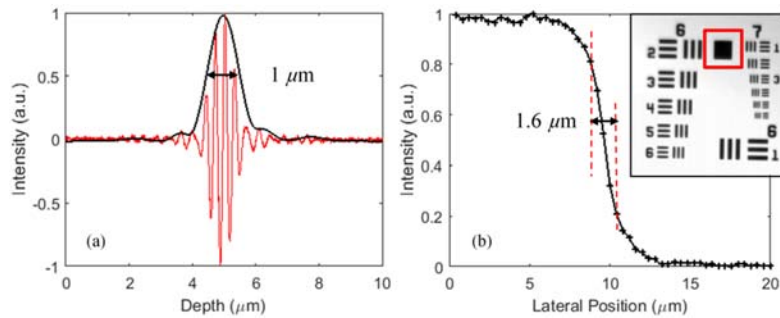
Fig. 3. Axial and lateral resolutions. (a) Measured axial response (red) and its corresponding tomography signal (black) demodulated by the proposed method, achieving an axial resolution of 1 μm and (b) a lateral resolution of 1.6 μm determined using a standard test target USAF 1951 (red box).

2.4 Material

In this study, all the fabrics were provided by "Center for Testmaterial B.V.". The samples were classed into two groups according to the color of cotton fabric substrates. As listed in Table. 1, the clean fabric substrate is labelled as CN-11 in group A and CN-17 in group B. The soiled sample in group A was stained by 50% beef fat and 50% lard with a red dye (CS-63S), whilst the soiled sample in group B was stained by used frying fat with a blue dye (CS-46B). The washed samples were washed with a detergent formulation at 20 and 40°C for 30 minutes.

Table 1. Measured cotton samples

	Photo	Clean/Soiled	Tag
Sample Group A		Clean	CN-11
		Washed at 40 °C	CS-63S@40
		Washed at 20 °C	CS-63S@20
		Soiled by 50% beef fat + 50% lard	CS-63S
Sample Group B		Clean	CN-17
		Washed at 40 °C	CS-46B@40
		Washed at 20 °C	CS-46B@20
		Soiled by Used Frying Fat	CS-46B

2.5 Colorimetric measurement

Standard colorimetric measurement was performed and quantified into CIELAB color space using a spectrophotometer (Color i7 X-rite) [1–3]. Stains removal can be then evaluated in terms of Euclidean distance, ΔE^*, taken as the difference of the measured L^*, a^*, and b^* values between clean and washed samples. L^* represents the lightness, while a^* represents the green to the red elements and b^* represents the blue to the yellow elements. Therefore, the lower is ΔE^*, the more effective is the washing. The stain removal index (SRI) is calculated as 100 minus ΔE^*, where 100 represents white (clean sample), thus, a higher SRI represents a cleaner fabric that is closer to white.

3. Results and discussion

3.1 Sub-surface measurement of cotton fabric samples

Colorimetry provides a simple, fast measurement of discriminating between clean, soiled and washed cotton fabric samples. However, it requires the sample to be dyed prior to measurement, e.g. red and blue colors applied in the study. Further, colorimetry technique cannot reveal the information on the effects of cleaning along the sample depth. Here, we investigate the feasibility of using OCT cross-sectional images (B-scans) to discriminate between the cleaning effect of the washed and unwashed fabrics. Figure 4 shows the high-resolution microscopic images with the FF-OCT focused on the sample surface, where woven fabric structure and micron-sized fibers can be seen. The woven fabric samples in the two groups are made up of interlaced yarns, and the diameter of the yarn is approximately 150 μm. Since tested samples have been soiled or washed, a region-of-interest (ROI) (shade/green region shown in Fig. 4) was selected along the weft yarn direction of the sample, which consists of 160×1000 pixels corresponding to an imaging area of 100×1000 μm^2. This allows a fine scanning up to 200 μm in air with a 5-nm scan step under a fast frame rate of 200 frames per second (fps). The resultant 3D datacube were reconstructed using the proposed method.
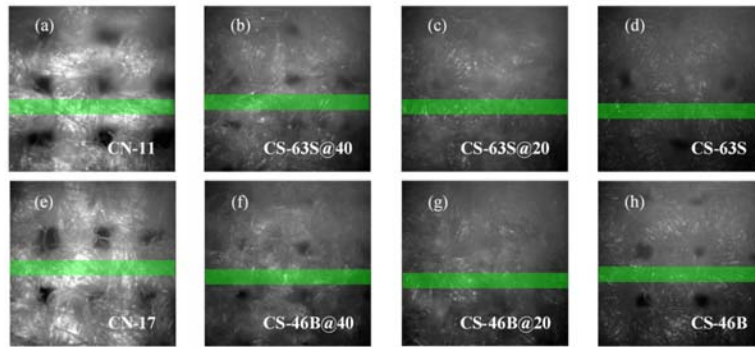

Fig. 4. Microscopic images corresponding to the fabric samples in each group taken from the sample arm of the FF-OCT. The region-of-interest where the depth-resolved scanning was performed is highlighted with shade/green.

Figures 5(a--e) and 5(g--k) show the representative B-scans images of the measured fabric samples in each group whilst Figs. 5(f) and 5(l) show their corresponding A-scan waveforms. The clean samples (CN-11/CN-17) exhibit structural layering with the strongest signal when compared to others. In contrast, for the soiled samples (CS-63S/CS-46B), nearly all the detected signals came from the sample surface, and the intensities of subsequent reflections are significantly reduced. After washing the soiled sample (CS-63S/CS-46B) under 20°C (CS-63S/CS-46B@20), a small amount of soil is removed, and micron-size fibres can be resolved at the sub-surface level with increased intensity. It is well-known that when cleaning is performed at an elevated temperature, increased soil removal can be achieved. This, therefore, explains why the measurement from the 40°C-washed sample (CS-63S/CS-46B@40) demonstrate an increased signal intensity when compared against the same sample but washed at 20°C. In summary, both the B-scan images and the A-scan waveforms suggest that the number of sub-surface structures is a good indicator of the cleaning effect: the higher the number, the cleaner the sample (or the less the remaining soils in a sample).
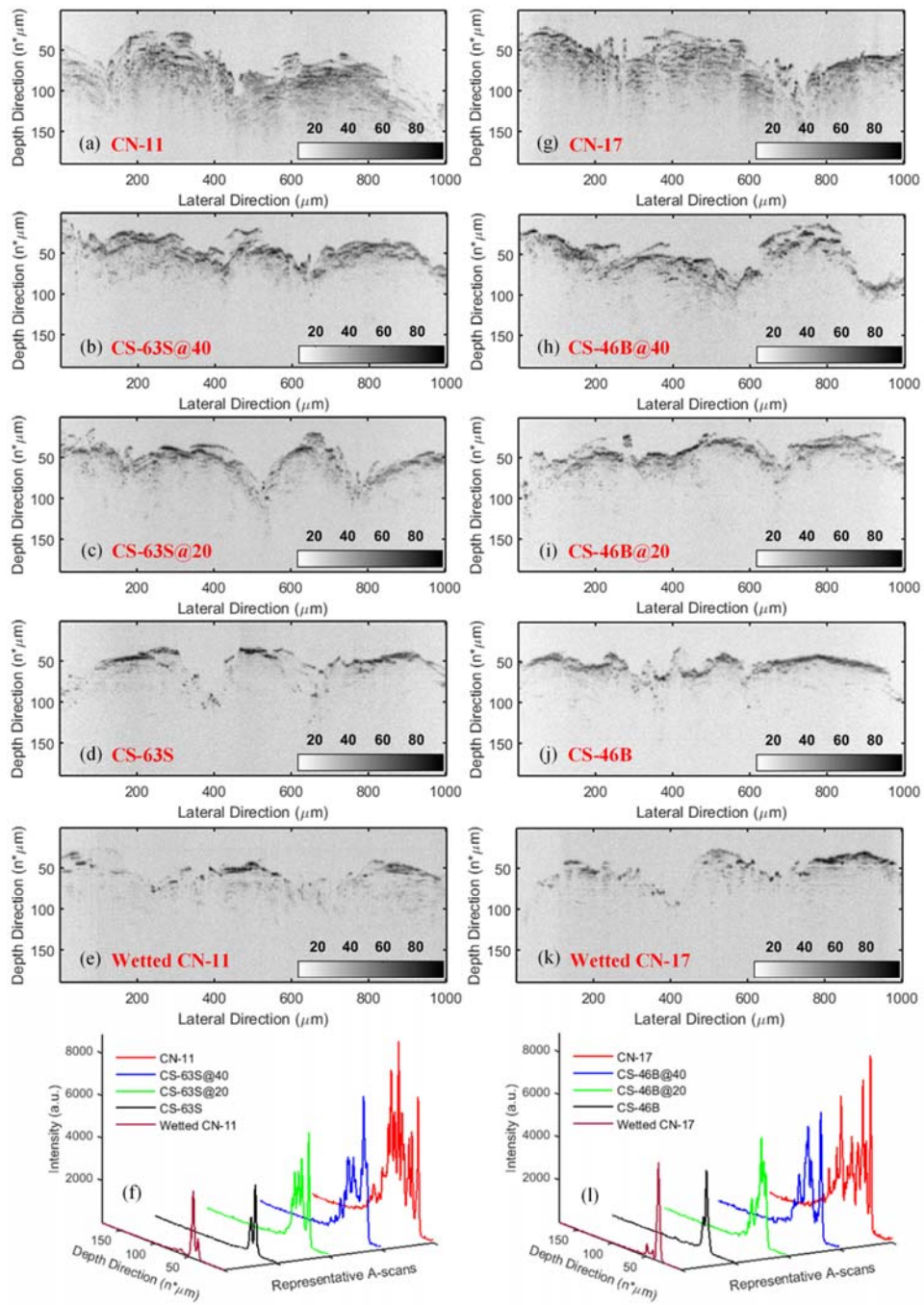
Fig. 5. Sub-surface imaging of the fabric samples in the two groups showing OCT measurements with cross-sectional images (B-scans) and depth profiles (A-scans), where the representative B-scans are selected from their correspondingly reconstructed 3D datacube, and the representative A-scans are extracted from their corresponding B-scans. (a–e) and (f) are the B-scan and the A-scan results of the samples in group A. (g–k) and (l) are the B-scan and the A-scan results of the samples in group B. Note that, (e) and (k) are the B-scans of the clean samples in wet state.

As shown in Fig. 5, both the clean and the soiled samples show a limited penetration depth of less than 70 μm, accounting for approximately 50% of the entire fabric thickness. This is mainly determined by the strong scattering of the fabric sample where there is a significant number of pores or air gaps between the interlocked fibres and fibrils that act as strong scatters. On the other hand, these air gaps also provide optical pathways for some light to reach the 'scatter' below the surface. The strong scattering from air–fabric structures leads to relatively large detectable OCT signals even from deeper fabric interfaces. For the soiled samples, firstly, scattering losses are reduced because of the reduced refractive index mismatch between the stain and fabric (as compared with air–fabric). This in principle should lead to a larger penetration depth. However, this reduced scattering will also lead to reduced OCT signal, making it more difficult to be detected by the FF-OCT particularly for the scattered light from deeper structures. Secondly, the stains may absorb the light or block the optical pathway, thus making the light more difficult to reach the deeper fabric interface and/or the scattered light more difficult to reach the OCT device. Consequently, no significant sub-surface features can be observed in the acquired B-scan images. In addition, due to the relatively high-NA microscope objective and specific design details of the experimental setup (no dynamic focus correction) there is an additional mechanism that will limit the penetration depth. As material with a refractive index $\neq 1$ is imaged into the interferometric probe depth moves up compared to the expected location (n = 1) whereas the focus position moves down. The result is the image of the depth location being interferometrically probed becomes blurred, when this blurring becomes comparable to or larger than the spatial coherence of the illuminating light, the interferometric signal will be attenuated. Future method developments of statically optimizing focus position or dynamic focus correction, would be expected to increase the penetration depths, particularly for heavily soiled or wet samples.

In order to further understand the underlying mechanisms of observed correlation between the measured OCT signal and the fabric cleanliness, additional measurements were performed on wetted fabric samples. By wetting the clean fabric sample sufficiently, the pores and air gaps within the fabric samples will be filled with water, leading to decreased refractive index mismatch thus reduced scattering (air–fabric vs. water–fabric). As shown in Figs. 5(e) and 5(k), the obtained B-scan images are indeed similar to strongly soiled fabric samples, suggesting that the scattering plays an important role in the observed correlation between the measured OCT signals and the cleanliness of the sample. Of course, some stains may absorb the light or block the optical pathway and its impact on the measured OCT signal should also be considered.

3.2 OCT based cleaning effect analysis

In order to investigate the feasibility of using OCT measurement to assess cleaning effect, we propose here a method based on the analysis of the volume taken up by the detectable sub-surface fibres. In particular, the volume can be obtained with the following steps
   1) Threshold setting for isolating imaged fibres from background;
   2) Labelling surface area through A-scan based signal analysis;
   3) Calculating the volume of the fibres detected below surface area.
Firstly, segmentation threshold was determined from the reconstructed 3D datacubes of clean, soiled and washed samples, respectively, where Otsu's method was used [35]. As a result, the area which only includes imaged fibres was isolated. Secondly, the fabric surface region was marked in each 3D image by finding the first peak positions of the A-scan signals involved in the analysed 3D datacube. Consequently, the volume occupied by the detectable fibres beneath the marked surface was calculated with known lateral and axial pixel size.

Figure 6 shows the fibre covered area and the marked surface area with red of the imaged fabric samples in group A and B. It can be seen that there are a high number of micron-sized fibres detected beneath the surface of the clean sample. In contrast, signals that reflected from the sub-surface fibres of the soiled sample are noticeably weaker. With an increase in washing condition, sub-surface fibres became increasingly noticeable. This is compared against the SRI

which is estimated based on measured L^*, a^* and b^* values (see Table. 2). Moreover, Figure 7 shows a good correlation between the volume and the SRI, thus demonstrating that the FF-OCT system could be a suitable alternative for inspecting the cleanliness of fabric sample.
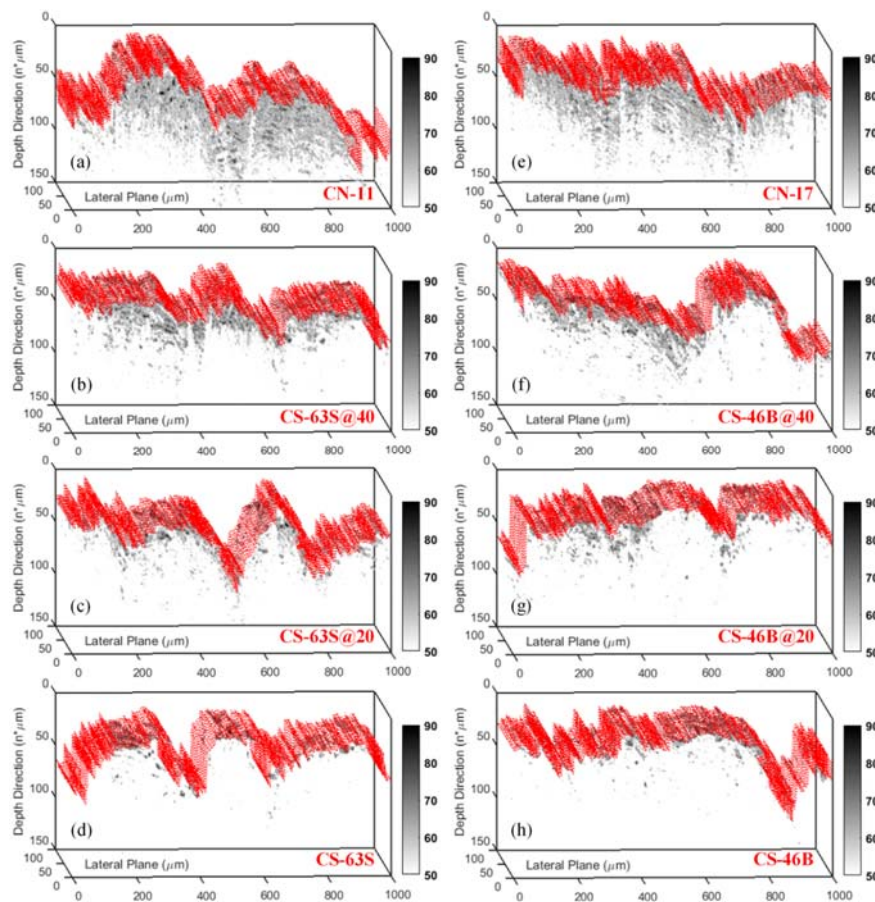

Fig. 6. Marked surface area (red) and detectable sub-surface fibres of the imaged fabric samples in the two groups. (a–d) and (e–h) are the results corresponding to the samples in group A and group B, respectively.

Table 2. Colorimetric measurement result and stain removal index of the fabric samples after washing with a detergent formulation at 20 and 40 ℃

	Fabric Sample	L^*		a^*		b^*		ΔE^*	SRI
		$\overline{x}^a$	SD^b	$\overline{x}$	SD	$\overline{x}$	SD		
Group A	CN-11	95.47	0.04	-0.30	0.01	2.68	0.04	/	100
	CS-63S@40	72.45	0.43	38.43	0.73	7.55	0.25	45.32	54.68
	CS-63S@20	66.64	0.89	47.38	1.44	12.50	0.79	56.58	43.42
Group B	CN-17	95.39	0.01	-0.34	0.01	2.92	0.04	/	100
	CS-46B@40	70.34	0.24	6.81	0.10	-20.28	0.38	34.88	65.12
	CS-46B@20	68.35	0.39	8.21	0.30	-24.72	0.56	39.60	60.40

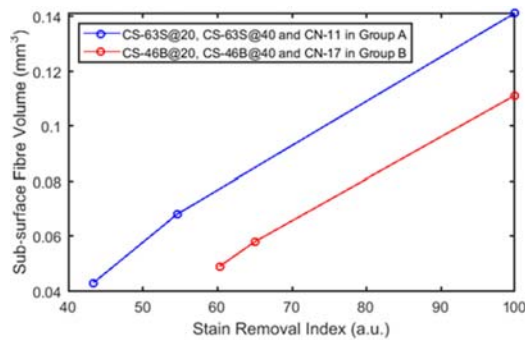[a] Mean value of 5 measuremnts   [b] Stardard deviation

Fig. 7. Cleaning effects demonstrated by detectable sub-surface fibre volume related to FF-OCT measurement and stain removal index related to colorimetric measurement.

To further show that FF-OCT does not require dying the sample, Figure 8 shows the B-scans of fabric samples treated with the same soils but without any dyes applied, where there are no obvious differences compared to the B-scan images of the dyed soiled samples. This suggests that the proposed FF-OCT method can be used to measure the stain removal of fabric sample without the need of dying process.
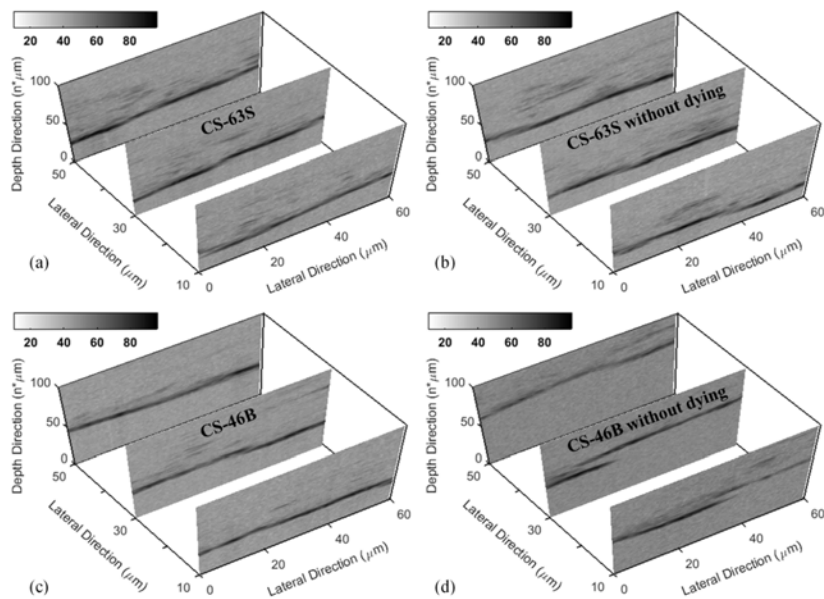

Fig. 8. Comparison measurement between the soiled samples with and without dying. (a) and (b) the B-scan maps of the soiled sample CS-63S and its corresponding non-dye sample. (c) and (d) the B-scan maps of the soiled sample CS-46B and its corresponding non-dye sample. Each measurement is performed to obtain a 3D datacube with the size of $60 \times 60 \times 100 \ \mu m^3$, and the B-scans are extracted from the reconstructed 3D datacubes.

In current wash studies, a white fabric is usually used as the substrate for assessing the effectiveness of detergent. The fabric is stained with a soil and the effectiveness of the detergent is measured by how closely the after-wash color gets back to white color of the fabric. For naturally colored stains such as tomato and curry sauce, the removal of them from the white fabric is highly visible. However, for other stains such as sunflower oil and butter stains, these may not be clearly visible on the white fabric although present on the fabric. In order to visualize the required stains, pigments or dyes are used for example violet dyes is used to visualize beef fat or vegetable oil on white fabric. Even though the chosen dyes are soluble in the stains or the

soils that are investigated, it is generally difficult to confirm if the dyes do not become separated from, and behave independently to, the stains during the cleaning process. The assessment of the effectiveness of a detergent by means of color difference is therefore an indirect method of assessment since what is being directly measured is effectively the removal of the dyes, not necessarily the actual staining agent.

The proposed FF-OCT method, even though is not ideal in taking over stain removal measurement in its current form because of the number of ingredients and stains used in a typical stain removal study. It can nevertheless be used as a complimentary method of measuring stain removal. It is envisaged that once several ingredients and formulations against several stains are screened, the proposed FF-OCT method can be used to confirm the findings on a smaller selection of stains and formulation as it is a direct method of measuring stain removal rather than an indirect (colorimetry) method. This potentially opens up a method of measuring real-life stains without the need for pigmentation or dyes currently applied.

4. Conclusion

In this study, we have demonstrated the use of sub-surface information obtained from FF-OCT to discriminate between clean, soiled and washed cotton fabrics. In particular, by achieving axial and lateral resolutions of about 1 μm and 1.6 μm, respectively, the micron-sized fibres/fibrils consisting of the cotton fabric can be resolved. The fibres, which can be detected from the sub-surface area, enables the assessment of the cleaning effect for the washed samples. A stain removal assessment method has been designed by analysing the reconstructed 3D datacube. The volume of the detectable sub-surface fibres in turn can be used to evaluate the cleaning effect related to the FF-OCT measurement.

Funding

References

1. G. van Dalen, A. Don, J. Veldt, E. Krijnen, and M. Gribnau, "Colour analysis of inhomogeneous stains on textile using flatbed scanning and image analysis," in Conference on Colour in Graphics, Imaging, and Vision, (Society for Imaging Science and Technology, 2008), pp. 53–57.
2. E. Ilec, B. Simončič, and A. Hladnik, "Evaluation of surfactant detergency using statistical analysis," Text. Res. J. **79**(4), 318–325 (2009).
3. S. Shivaji Biranje, A. Nathany, N. Mehra, and R. Adivarekar, "Optimisation of detergent ingredients for stain removal using statistical modelling," J. Surfactants Deterg. **18**(6), 949–956 (2015).
4. A. K. R. Choudhury, "Colour-difference assessment," in Principles of Colour and Appearance Measurement, M. L. Gulrajani, eds. (Elsevier, 2014).
5. D. Huang, E. A. Swanson, C. P. Lin, J. S. Schuman, W. G. Stinson, W. Chang, M. R. Hee, T. Flotte, K. Gregory, and C. A. Puliafito, "Optical coherence tomography," Science **254**(5035), 1178–1181 (1991).
6. H. Liang, M. G. Cid, R. G. Cucu, G. Dobre, A. G. Podoleanu, J. Pedro, and D. Saunders, "En-face optical coherence tomography-a novel application of non-invasive imaging to art conservation," Opt. Express **13**(16), 6133–6144 (2005).
7. H. Liang, R. Lange, H. Howard, and J. Spooner, "Non-invasive investigations of a wall painting using optical coherence tomography and hyperspectral imaging," Proc. SPIE **8084**, 80840F (2011).
8. J. P. Dunkers, R. S. Parnas, C. G. Zimba, R. C. Peterson, K. M. Flynn, J. G. Fujimoto, and B. E. Bouma, "Optical coherence tomography of glass reinforced polymer composites," Compos. Part A Appl. Sci. Manuf. **30**(2), 139–145 (1999).
9. J. P. Dunkers, F. R. Phelan, D. P. Sanders, M. J. Everett, W. H. Green, D. L. Hunston, and R. S. Parnas, "The application of optical coherence tomography to problems in polymer matrix composites," Opt. Lasers Eng. **35**(3), 135–147 (2001).
10. M. D. Duncan, M. Bashkansky, and J. Reintjes, "Subsurface defect detection in materials using optical coherence tomography," Opt. Express **2**(13), 540–545 (1998).
11. M. Bashkansky, M. Duncan, M. Kahn, D. Lewis, and J. Reintjes, "Subsurface defect detection in ceramics by high-speed high-resolution optical coherent tomography," Opt. Lett. **22**(1), 61–63 (1997).

12. S. Zhong, Y. -C. Shen, L. Ho, R. K. May, J. A. Zeitler, M. Evans, P. F. Taday, M. Pepper, T. Rades, and K. C. Gordon, "Non-destructive quantification of pharmaceutical tablet coatings using terahertz pulsed imaging and optical coherence tomography," Opt. Lasers Eng. **49**(3), 361–365 (2011).
13. C. Li, J. A. Zeitler, Y. Dong, and Y. -C. Shen, "Non-destructive evaluation of polymer coating structures on pharmaceutical pellets using full-field optical coherence tomography," J. Pharm. Sci. **103**(1), 161–166 (2014).
14. H. Lin, Y. Dong, D. Markl, B. M. Williams, Y. Zheng, Y. -C. Shen, J. A. Zeitler, "Measurement of the Intertablet Coating Uniformity of a Pharmaceutical Pan Coating Process With Combined Terahertz and Optical Coherence Tomography In-Line Sensing," J. Pharm. Sci. **106**(4), 1075–1084 (2017).
15. J. Zhang, B. M. Williams, S. Lawman, D. Atkinson, Z. Zhang, Y. Shen, and Y. Zheng, "Non-destructive analysis of flake properties in automotive paints with full-field optical coherence tomography and 3D segmentation," Opt. Express **25**(16), 295543 (2017).
16. Y. Dong, S. Lawman, Y. Zheng, D. Williams, J. Zhang, and Y.-C. Shen, "Nondestructive analysis of automotive paints with spectral domain optical coherence tomography," Appl. Opt. **55**(13), 3695–3700 (2016).
17. K. A. Serrels, M. K. Renner, and D. T. Reid, "Optical coherence tomography for non-destructive investigation of silicon integrated-circuits," Microelectron. Eng. **87**(9), 1785–1791 (2010).
18. A. G. Podoleanu, "Optical coherence tomography," Br. J. Radiol. **78**(935), 976–988 (2005).
19. E. Beaurepaire, A. C. Boccara, M. Lebec, L. Blanchot, and H. Saint-Jalmes, "Full-field optical coherence microscopy," Opt. Lett. **23**(4), 244–246 (1998).
20. B. Laude, A. De Martino, B. Drevillon, L. Benattar, and L. Schwartz, "Full-field optical coherence tomography with thermal light," Appl. Opt. **41**(31), 6637–6645 (2002).
21. I. Abdulhalim, "Spatial and temporal coherence effects in interference microscopy and full-field optical coherence tomography," Ann. Phys. **524**(12), 787–804 (2012).
22. I. Abdulhalim, "Competence between spatial and temporal coherence in full field optical coherence tomography and interference microscopy," J. Opt. A: Pure Appl. Opt. **8**, 952–958 (2006).
23. A. Safrani and I. Abdulhalim, "Spatial coherence effect on layer thickness determination in narrowband full-field optical coherence tomography," Appl. Opt. **50**(18), 3021–3027 (2011).
24. O. Sasaki, H. Okazaki, and M. Sakai, "Sinusoidal phase modulating interferometer using the integrating-bucket method," Appl. Opt. **26**(6), 1089–1093 (1987).
25. A. Dubois, K. Grieve, G. Moneron, R. Lecaque, L. Vabre, and C. Boccara, "Ultrahigh-resolution full-field optical coherence tomography," Appl. Opt. **43**(14), 2874–2883 (2004).
26. E. Bordenave, E. Abraham, G. Jonusauskas, N. Tsurumachi, J. Oberle, C. Rulliere, P. Minot, M. Lassegues, and J. S. Bazeille, "Wide-field optical coherence tomography: imaging of biological tissues," Appl. Opt. **41**(10), 2059–2064 (2002).
27. A. Dubois, L. Vabre, A.-C. Boccara, and E. Beaurepaire, "High-resolution full-field optical coherence tomography with a Linnik microscope," Appl. Opt. **41**(4), 805–812 (2002).
28. M. Akiba, K. Chan, and N. Tanno, "Full-field optical coherence tomography by two-dimensional heterodyne detection with a pair of CCD cameras," Opt. Lett. **28**(10), 816–818 (2003).
29. M. Sato, T. Nagata, T. Niizuma, L. Neagu, R. Dabu, and Y. Watanabe, "Quadrature fringes wide-field optical coherence tomography and its applications to biological tissues," Opt. Commun. **271**(2), 573–580 (2007).
30. L.B, Liu, J. A. Gardeki, S. K. Nadkarni, J. D. Toussaint, Y. Yagi, B. E. Bouma, G. J. Tearney, "Imaging the subcellular structure of human coronary atherosclerosis using micro–optical coherence tomography," Nat. Med **17**, 1010–1014 (2011).
31. W. Drexler, "Ultrahigh-resolution optical coherence tomography," J Biomed Opt **9**(1), 47–74 (2004).
32. C. Tay, C. Quan, and M. Li, "Investigation of a dual-layer structure using vertical scanning interferometry," Opt. Lasers Eng. **45**(8), 907–913 (2007).
33. J. A. Izatt, M. A. Choma and A. Dhalla, "Theory of Optical Coherence Tomography," in *Optical Coherence Tomography Technology and Applications*, W. Drexler, and J. G. Fujimoto, eds. (Springer, 2008).
34. C. Akcay, P. Parrein, and J. P. Rolland, "Estimation of longitudinal resolution in optical coherence imaging," Appl. Opt. **41**(25), 5256–5262 (2002).
35. N. Otsu, "A threshold selection method from gray-level histograms," IEEE Trans. Syst. Man Cybern. **9**(1), 62–66 (1979).